Nano Research 2016, 9(8): 2338–2346
DOI 10.1007/s12274-016-1120-z
Research Article
ISSN 1998-0124
CN 11-5974/O4

$Pt/Y_2O_3:Eu^{3+}$ composite nanotubes: Enhanced photoluminescence and application in dye-sensitized solar cells

Mingqi Yu[1], Jiamin Su[1], Guofeng Wang[1] (✉), and Yadong Li[2]

[1] *Key Laboratory of Functional Inorganic Material Chemistry, Ministry of Education, School of Chemistry and Materials Science, Heilongjiang University, Harbin 150080, China*
[2] *Department of Chemistry, Tsinghua University, Beijing 100084, China*

Received: 25 March 2016
Revised: 21 April 2016
Accepted: 22 April 2016

KEYWORDS
$Pt/Y_2O_3:Eu^{3+}$,
nanocrystals,
luminescence,
dye-sensitized solar cells

ABSTRACT

$Y(OH)_3:Eu^{3+}$ nanotubes were synthesized using a facile hydrothermal method, and then, Pt particles were grown on the surface of the nanotubes using a combination of vacuum extraction and annealing. The resulting $Pt/Y_2O_3:Eu^{3+}$ composite nanotubes not only exhibited enhanced red luminescence under 255- or 468-nm excitation but could also be used to improve the efficiency of dye-sensitized solar cells, resulting in an efficiency of 8.33%, which represents a significant enhancement of 11.96% compared with a solar cell without the composite nanotubes. Electrochemical impedance spectroscopy results indicated that the interfacial resistance of the TiO_2–dye|I_3^-/I^- electrolyte interface of the TiO_2–$Pt/Y_2O_3:Eu^{3+}$ composite cell was much smaller than that of a pure TiO_2 cell. In addition, the TiO_2–$Pt/Y_2O_3:Eu^{3+}$ composite cell exhibited a shorter electron transport time and longer electron recombination time than the pure TiO_2 cell.

1 Introduction

Luminescent materials, also known as phosphors, are defined as solids that can absorb and convert certain types of energy into light radiation [1]. Recently, luminescence-based techniques have continued to attract considerable attention because of their wide potential in the fields of optical devices and biomedicine, such as displays, immunoassays, and anti-counterfeiting [2–4]. In particular, luminescent inorganic nanomaterials have attracted considerable interest because of their tremendous potential applications and for fundamental science research in many fields [5]. Among all the types of inorganic nanomaterials, rare-earth (RE) materials are some of the most important and attractive candidates [6, 7]. RE elements always exist as trivalent cations, composed of the 15 lanthanides (from lanthanum to lutetium) in addition to scandium and yttrium. Lanthanide (Ln) ions have abundant f-orbital configurations and can exhibit sharp fluorescent emissions via intra-4f or 4f–5d transitions; thus, these ions are widely used as emitting species

Address correspondence to wanggf_w@163.com

in many phosphors [8]. In terms of the mechanism of luminescence, RE luminescence can be divided into down-conversion and up-conversion emission processes [9]. The down-conversion process is the conversion of higher-energy photons into lower-energy photons, which often requires two main components, an inorganic matrix (known as the host) and activated Ln^{3+} doping ions (activators) [10, 11].

Many types of inorganic compounds, such as oxides, fluorides, phosphates, and vanadates, have been widely used as host materials [12–15]. Among these materials, Y_2O_3 offers good chemical and photochemical stability, a high melting point, and, most importantly, can be easily doped. Y_2O_3 doped with trivalent europium ions (Y_2O_3:Eu^{3+}) is a well-known red-emitting phosphor used in cathode ray tubes, fluorescent lamps, and projection television tubes [16]. For luminescent materials, Y_2O_3:Eu^{3+} not only exhibits a sharp emission bandwidth, high photostability, and long lifetime but can also combine with some compounds [17] such as Y_2O_3:Yb, Er@mSiO_2–Cu_xS for enhanced chemophotothermal anti-cancer therapy and dual-modal imaging [18]. Metal-induced photoluminescence enhancement or quenching have potential applications in sensing technologies and solid-state lighting using materials such as Ag@SiO_2@Y_2O_3:Er^{3+} and Au/Y_2O_3:Eu^{3+} [19, 20]. However, Pt/Y_2O_3:Eu^{3+} composite nanotubes have never been reported.

Dye-sensitized solar cells (DSSCs) have attracted considerable attention since the innovative report in 1991 [21], which resulted in revolutionary innovation in the development of photoelectrochemical cells and provided a new method of using solar energy as a result of their high power conversion, low cost, and environmentally friendliness. It is well known that the photoelectric conversion efficiency of DSSCs can be enhanced by improving the photoanode, sensitizers, and electrolytes [22–35]. In particular, the photoanode plays an important role in electron–hole separation, dye adsorption, and electronic transmission.

Herein, we have successfully synthesized enhanced luminescent Pt/Y_2O_3:Eu^{3+} composite nanotubes, which have the ability to improve the efficiency of solar cells. The electron transport and interfacial recombination kinetics were investigated using electrochemical impedance spectroscopy (EIS) and intensity-modulated photocurrent spectroscopy (IMPS) and intensity-modulated photovoltage spectroscopy (IMVS).

2 Experimental

2.1 Sample preparation

Analytical-grade $Ln(NO_3)_3{\cdot}6H_2O$ (Ln = Y and Eu), NaOH, and H_2PtCl_6 were obtained from Beijing Chemical Reagents, China. All of the chemicals used in this paper were of analytical grade and used without further purification.

The $Y(OH)_3$:Eu^{3+} nanotubes were prepared according to our previous report using a typical hydrothermal method [36]. For the synthesis of the Pt/Y_2O_3:Eu^{3+} composite nanotubes, the as-prepared $Y(OH)_3$:Eu^{3+} nanotubes (0.14 g) were placed into a suction bottle; then, the bottle was sealed using a dropping funnel with some H_2PtCl_6 (0.02 M) aqueous solution. After the suction bottle maintained a vacuum for 30 min, the solution was added dropwise to the suction bottle until the solution was fully infused into the $Y(OH)_3$:Eu^{3+} nanotubes. Then, the mixture was poured into a 50-mL beaker, dried in a vacuum at 80 ℃ for 24 h, and finally sintered at 600 ℃ for 2 h.

2.2 Materials characterization

The crystal structure was analyzed using a Rigaku D/MAX-rA X-ray diffractometer (Japan) equipped with graphite monochromatized Cu Kα radiation (λ = 1.541874 Å) using an operating voltage and current of 40 kV and 40 mA, respectively. The size and morphology of the final products were determined using scanning electron microscopy (SEM, JSM-6301F) and transmission electron microscopy (TEM, JEOL JEM-2010F) at 200 kV. X-ray photoelectron spectroscopy (XPS) analysis was performed on a VG ESCALABMK II with a Mg KR (1,253.6 eV) achromatic X-ray source.

The photoluminescence spectra were recorded with a Hitachi F-4600 fluorescence spectrophotometer at room temperature. To compare the luminescence properties of different samples, the luminescence spectra were measured using the same instrument parameters (a slit width of 2.5 nm and a photomultiplier voltage of 400 V).

2.3 Fabrication of photoelectrodes

Several pastes were prepared from homogeneously mixing Pt/Y_2O_3:Eu^{3+} and TiO_2 (Degussa P25) into 1.5 mL of a TiO_2 colloid. The TiO_2 colloid was prepared following a previously published synthesis procedure [37]. A screen-printed double layer of TiO_2–Pt/Y_2O_3:Eu^{3+} was used as the photoanode. The first layer of TiO_2–Pt/Y_2O_3:Eu^{3+} was prepared using the doctor-blade method on a fluorine-doped tin oxide (FTO) substrate and then sintered at 450 ˚C for 30 min. Subsequently, the first TiO_2–Pt/Y_2O_3:Eu^{3+} film was covered with a second layer of TiO_2–Pt/Y_2O_3:Eu^{3+} before sintering at 450 ˚C for 30 min. Sensitization of the photoelectrodes was achieved by immersing them into 0.5 mM $((C_4H_9)_4N)_2$[Ru(4-carboxy-4′-carboxylate-2,2′ bipyridine)$_2$$(NCS)_2$] dye (N719, Solaronix SA, Switzerland) in acetonitrile and tert-butanol (volume ratio of 1:1) for 48 h at room temperature. Pt counter electrodes were prepared following a method previously reported in the literature [38]. The dye-sensitized photoanode was assembled with a Pt counter electrode into a sandwich-type cell. The sandwich-type cell was further fixed together with epoxy resin. The space between the electrodes was filled with the electrolyte, which consisted of 0.6 M 1-propyl-2,3-dimethyl-imidazolium iodide, 0.05 M I_2, 0.1 M LiI, and 0.5 M tert-butylpyridine in 3-methoxypropionitrile, by capillary action.

2.4 Photovoltaic properties

Photovoltaic measurements were performed using a solar simulator (Oriel, USA) equipped with an AM 1.5G radiation (1 sun conditions, 100 mW·cm^{-2}) filter as the light source. The irradiation area of the DSSCs was 0.09 cm^2. The EIS measurements were performed with a computer-controlled IM6 impedance measurement unit (Zahner Elektrik, Germany) by applying sinusoidal perturbations of 10 mV with a bias of –0.8 V in the frequency range from 10 mHz to 1 MHz. The obtained spectra were fitted using ZsimpWin software in terms of appropriate equivalent circuits. The electron transport and recombination properties were measured using IMPS and IMVS (Zahner Elektrik, Germany). The DSSCs were probed through the photoanode side with a frequency response analyzer using a white-light-emitting diode (wlr-01) as the light source. The frequency range was 0.1–1,000 Hz, and the irradiated intensity was varied from 30 to 150 W·m^{-2}.

3 Results and discussion

3.1 Sample crystal structures and morphologies

The crystal structure, particle size, and morphologies of the products were determined using X-ray diffraction (XRD), TEM, and SEM. Figure 1 presents the XRD patterns of Pt/Y_2O_3:Eu^{3+} composite nanotubes with different Ln^{3+}:Pt^+ mole ratios. From bottom to top, the ratios increased. The peaks in Fig. 1 marked by an asterisk (*) arise from cubic Pt particles (JCPDS 87-0646). The other diffraction peaks can be indexed to the cubic phase Y_2O_3:Eu^{3+} (JCPDS 86-1326). The XRD pattern of the cubic phase Pt was only observed when the Ln^{3+}:Pt^+ mole ratio was larger than 1:0.2. When the Ln^{3+}:Pt^+ mole ratio was 1:0.5, the XRD pattern of Y_2O_3:Eu^{3+} almost vanished.

Figure 2 presents a TEM image of $Y(OH)_3$:Eu^{3+} and Pt/Y_2O_3:Eu^{3+} (Ln^{3+}:Pt^+ = 1:0.2). The Pt/Y_2O_3:Eu^{3+} nanocrystals are uniform, tube-like, and similar to the $Y(OH)_3$:Eu^{3+} nanotubes. In addition, some Pt fragments are present on the surface of the Y_2O_3:Eu^{3+} nanotubes. Further detailed component analysis of the Pt/Y_2O_3:Eu^{3+} was performed using high-resolution transmission electron microscopy (HRTEM), and the results are presented in Figs. 2(c) and 2(d). The typical HRTEM

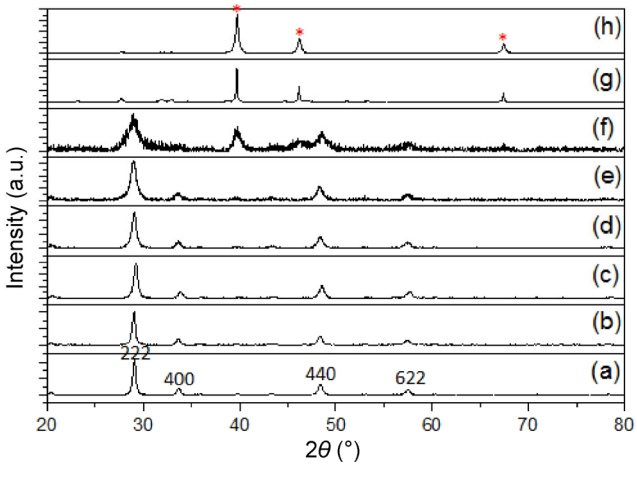

Figure 1 XRD patterns of Pt/Y_2O_3:Eu^{3+} composite nanotubes with different Ln^{3+}:Pt^+ mole ratios: (a) 1:0.001, (b) 1:0.01, (c) 1:0.02, (d) 1:0.04, (e) 1:0.1, (f) 1:0.2, (g) 1:0.5, and (h) 1:1.

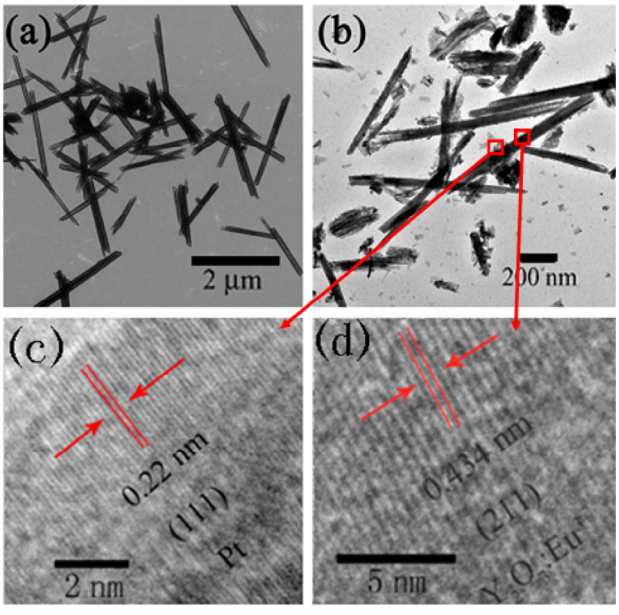

Figure 2 TEM and HRTEM images of (a) $Y(OH)_3:Eu^{3+}$ and (b)–(d) $Pt/Y_2O_3:Eu^{3+}$ composite nanotubes.

images of a single composite nanotube reveal two interplanar spacings of 0.434 and 0.22 nm, corresponding to the ⟨211⟩ plane of the $Y_2O_3:Eu^{3+}$ cubic phase and the ⟨111⟩ plane of the Pt cubic phase, respectively. These results indicate that $Y_2O_3:Eu^{3+}$ and Pt coexist in the $Pt/Y_2O_3:Eu^{3+}$ composite nanotubes.

To further demonstrate the coexistence of $Y_2O_3:Eu^{3+}$ and Pt in the composite nanotubes, $Pt/Y_2O_3:Eu^{3+}$ composite nanotubes were examined using energy-dispersive X-ray spectroscopy (EDX) under SEM, and the results are presented in Fig. S1 in the Electronic Supplementary Material (ESM). The content of Pt in $Pt/Y_2O_3:Eu^{3+}$ was ~7.45 wt.% for $Ln^{3+}:Pt^{+} = 1:0.02$.

Figure 3 presents the XPS spectra of the $Pt/Y_2O_3:Eu^{3+}$ ($Ln^{3+}:Pt^{+} = 1:0.02$) composite nanotubes. The results also indicate that $Y_2O_3:Eu^{3+}$ and Pt coexist in the $Pt/Y_2O_3:Eu^{3+}$ composite nanotubes. The O 1s XPS spectra exhibit two peaks; the peak at higher binding energy can be attributed to the lattice oxygen, and the other peak can be attributed to surface chemisorbed oxygen. The Y 3d XPS spectra contain three peaks; the two main peaks are attributed to Y $3d_{5/2}$ and Y $3d_{3/2}$, and the smaller peak may be affected by the Pt particles on the surface of $Y_2O_3:Eu^{3+}$. The Pt 4f XPS spectra contain two peaks, which are attributed to $4f_{7/2}$ and $4f_{5/2}$.

3.2 Photoluminescence of $Y_2O_3:Eu^{3+}$ and $Pt/Y_2O_3:Eu^{3+}$

To investigate the structural difference between the Y_2O_3 and Pt/Y_2O_3 composite nanotubes, we doped both samples with Eu^{3+} and employed Eu^{3+} ions as structural probes to explore their surroundings. For comparison,

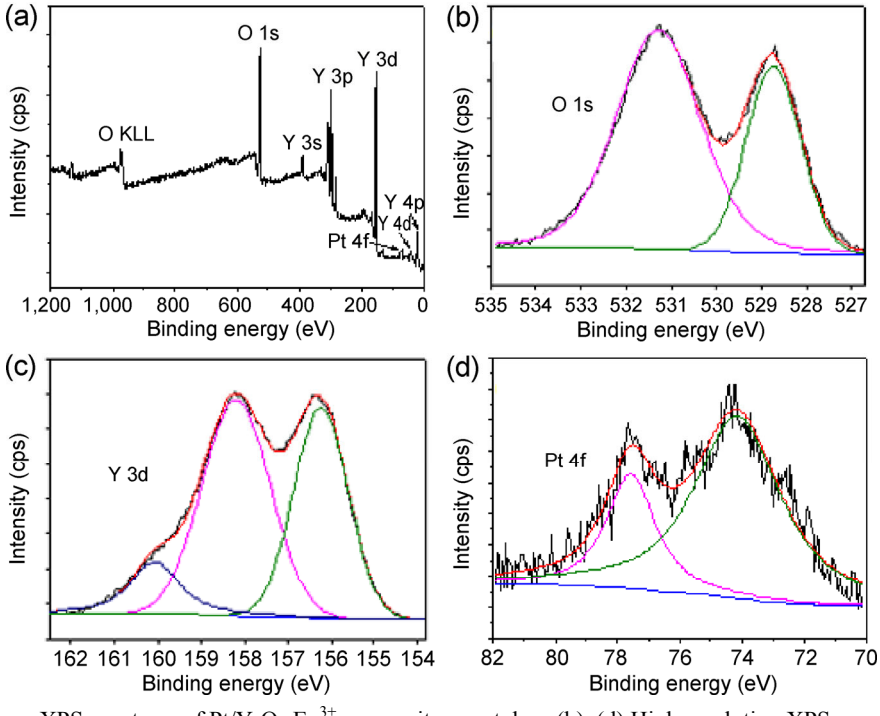

Figure 3 (a) The survey XPS spectrum of $Pt/Y_2O_3:Eu^{3+}$ composite nanotubes. (b)–(d) High resolution XPS spectra of O, Y, and Pt.

the luminescence properties of Y_2O_3:Eu^{3+} (without Pt) nanotubes was investigated first. Figure S2 in the ESM presents the room-temperature excitation spectra of Y_2O_3:Eu^{3+} (0.5%) nanotubes at various emission wavelengths. The broad band extending from 200 to 300 nm is assigned to the charge-transfer transitions from the 2p orbital of O^{2-} to the 4f orbital of Eu^{3+}, which is closely related to the covalency between O^{2-} and Eu^{3+} and the coordination environment around Eu^{3+}. The sharp lines in Fig. S2 (in the ESM) correspond to the $^7F_0 \rightarrow {}^5H_3$ (~332 nm), $^7F_0 \rightarrow {}^5D_4$ (~364 nm), $^7F_0 \rightarrow {}^5G_3$ (~383 nm), $^7F_0 \rightarrow {}^5L_6$ (~395 nm), $^7F_0 \rightarrow {}^5D_2$ (~468 nm), and $^7F_0 \rightarrow {}^5D_1$ (~534 nm) transitions of Eu^{3+} ions.

Figure S3 in the ESM presents the emission spectra of Y_2O_3:Eu^{3+} (0.5%) nanotubes excited at various wavelengths. The $^5D_0 \rightarrow {}^7F_0$ (~584 nm), $^5D_0 \rightarrow {}^7F_1$ (590–602 nm), $^5D_0 \rightarrow {}^7F_2$ (615–634 nm), and $^5D_0 \rightarrow {}^7F_3$ (~654 nm) transitions of Eu^{3+} ions were observed. The luminescence was dominated by the $^5D_0 \rightarrow {}^7F_2$ transition. The $^5D_0 \rightarrow {}^7F_1$ emission was split into three sub-bands because of the local fields around Eu^{3+} and their separations depend on the energy for the direct excitation from the $^7F_0$ ground level to the $^5D_0$ excited level.

Figure 4 presents the excitation spectra of Pt/Y_2O_3:Eu^{3+} with different Ln^{3+}:Pt^+ mole ratios. The intensity of the charge-transfer bands first increased and then decreased with increasing Pt content. Figure 5 presents the emission spectra of Pt/Y_2O_3:Eu^{3+} with different Ln^{3+}:Pt^+ mole ratios. The luminescence was

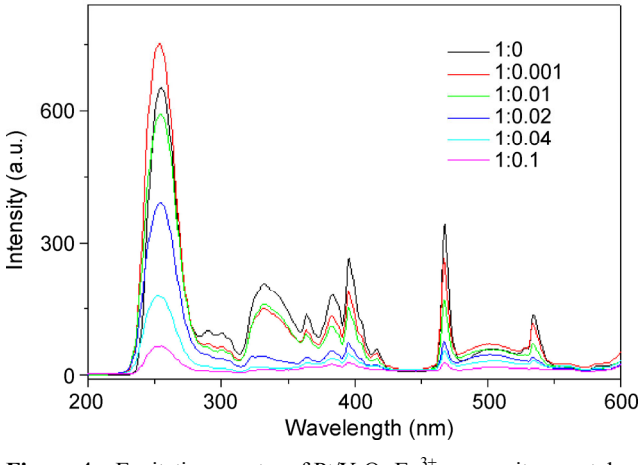

Figure 4 Excitation spectra of Pt/Y_2O_3:Eu^{3+} composite nanotubes with different Ln^{3+}:Pt^+ mole ratios monitored at 615 nm.

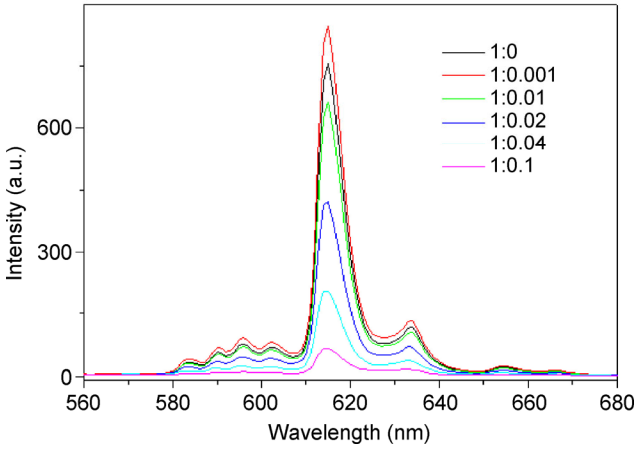

Figure 5 Emission spectra of Pt/Y_2O_3:Eu^{3+} composite nanotubes with various Ln^{3+}:Pt^+ mole ratios excited at 255 nm.

dominated by the $^5D_0 \rightarrow {}^7F_2$ transition. The photoluminescence was the strongest when the Ln^{3+}:Pt^+ mole ratio was 1:0.001.

Figure 6 presents the emission spectra of Pt/Y_2O_3:Eu^{3+} with different Pt contents excited at 395 nm. The $^5D_0 \rightarrow {}^7F_2$ emission at 634 nm was split into two sub-bands. The intensity ratio of the 615 nm to 634 nm emission decreased with increasing Pt content. Figure S4 in the ESM presents the emission spectra of Pt/Y_2O_3:Eu^{3+} with various Pt contents excited at 255 nm.

Figure 7 presents the luminescence decay curves for the Pt/Y_2O_3:Eu^{3+} composite nanotubes by monitoring the emission peak at 615 nm. Both the decay curves were fitted with a biexponential function, which led

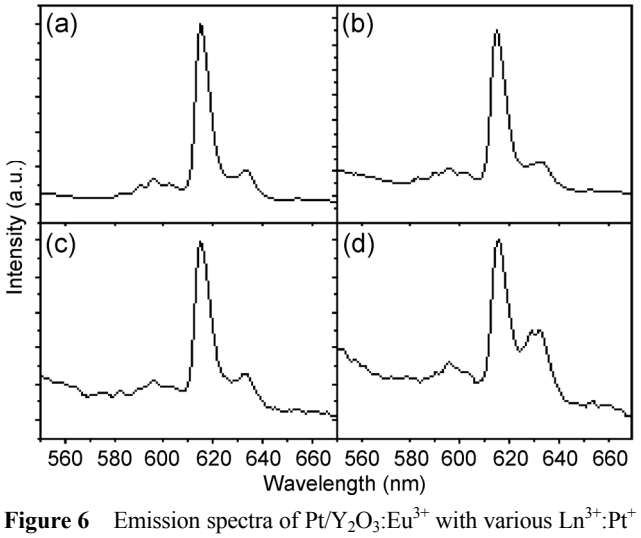

Figure 6 Emission spectra of Pt/Y_2O_3:Eu^{3+} with various Ln^{3+}:Pt^+ mole ratios excited at 395 nm: (a) 1:0.01, (b) 1:0.02, (c) 1:0.04, and (d) 1:0.1.

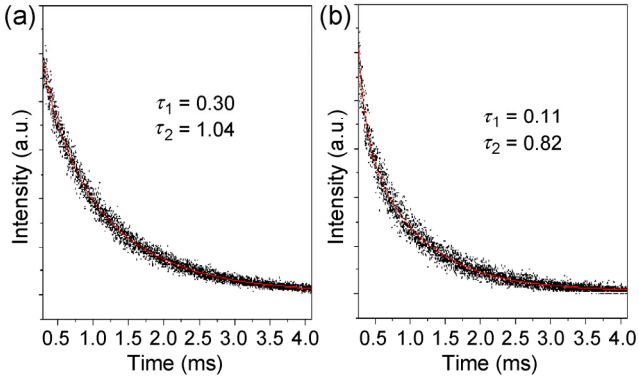

Figure 7 Luminescence decay curve for the Pt/Y_2O_3:Eu^{3+} composite nanotubes with Ln^{3+}:Pt^+ mole ratios of (a) 1:0.04 and (b) 1:0.1.

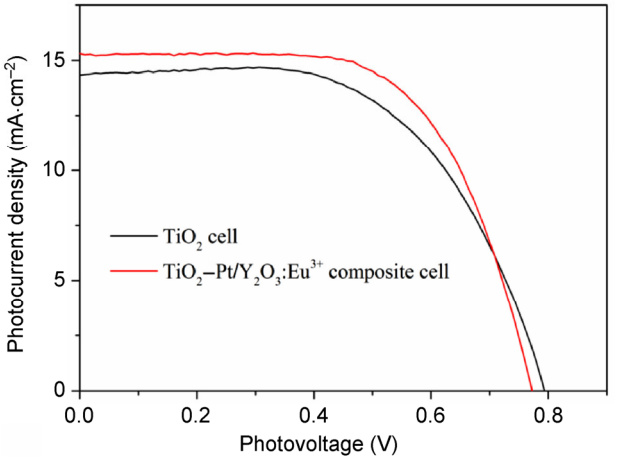

Figure 8 *J*–*V* curves of the pure TiO_2 cell and TiO_2–Pt/Y_2O_3:Eu^{3+} composite cells under simulated solar light radiation in the wavelength range of 400 nm ≤ λ ≤ 800 nm.

to two lifetimes: 0.30 and 1.04 ms for Pt/Y_2O_3:Eu^{3+} (Ln^{3+}:Pt^+ = 1:0.04) and 0.11 and 0.82 ms for Pt/Y_2O_3:Eu^{3+} (Ln^{3+}:Pt^+ = 1:0.1). The lifetimes decreased with increasing Pt content. We suggest that this change could be related to shorter Pt/Y_2O_3:Eu^{3+} composite nanotubes leading to an increase in the non-radiative transition rate.

3.3 Photoelectrochemical properties of TiO_2–Pt/Y_2O_3:Eu^{3+} composite DSSCs

To investigate the effects of TiO_2–Pt/Y_2O_3:Eu^{3+} on the photoelectric properties of DSSCs, DSSC prototype devices were fabricated using N719-sensitized TiO_2–Pt/Y_2O_3:Eu^{3+} composite electrodes. Figure 8 presents the photocurrent density–voltage (*J*–*V*) curves of the pure TiO_2 cell and TiO_2–Pt/Y_2O_3:Eu^{3+} composite cell. The corresponding values of the open-circuit voltage (V_{oc}), short-circuit current density (J_{sc}), fill factor (FF), and overall conversion efficiency (η), obtained from the curves of solar cells, are listed in Table 1. The results indicate that the photoelectric conversion efficiencies of the TiO_2–Pt/Y_2O_3:Eu^{3+} composite cells were higher than that of the pure TiO_2 cell. The best photoelectric conversion performance was achieved when the mass concentration of Pt/Y_2O_3:Eu^{3+} was 5%. The lower V_{oc} of the TiO_2–Pt/Y_2O_3:Eu^{3+} composite cells can be attributed to heavy doping effects. Heavy impurity doping causes a shift of the conduction and valence bands, yielding so-called band gap narrowing and resulting in a decrease of V_{oc}.

EIS is a powerful method to investigate the internal resistances of the charge-transfer process of DSSCs.

Table 1 Solar cell parameters of pure TiO_2 cell and TiO_2–Pt/Y_2O_3:Eu^{3+} composite cell under simulated solar light radiation in the wavelength range of 400 nm ≤ λ ≤ 800 nm

DSSCs	V_{oc} (V)	J_{sc} (mA·cm^{-2})	FF	η (%)
Pure TiO_2	0.79	14.33	0.59	7.44
TiO_2-Pt/Y_2O_3:Eu^{3+}	0.77	15.31	0.64	8.33

The wide frequency range of EIS means that the wide-scale internal resistances of each electrochemical step can be measured simultaneously. DSSCs are complex systems composed of several interfaces. A high level of electron accumulation must occur because photogenerated electrons are not extracted immediately at the electrode contact under illumination. Generally, the impedance at low frequency (0.05–1 Hz) refers to the Nernst diffusion of I_3^-/I^- within the electrolyte. The impedance at high frequency (1–100 kHz) corresponds to the capacitance and charge-transfer resistance at the Pt|I_3^-/I^- electrolyte interface. The medium-frequency response at 1–100 Hz is related to the photoelectrode–dye|I_3^-/I^- electrolyte interface, where the accumulation of photoelectrons and redox shuttles is expected. Figure 9 presents the EIS results of the pure TiO_2 cell and TiO_2–Pt/Y_2O_3:Eu^{3+} cell. The interfacial resistance of the TiO_2–dye|I_3^-/I^- electrolyte interface of the TiO_2–Pt/Y_2O_3:Eu^{3+} cell is much smaller than that of the pure TiO_2 cell.

The inset in Fig. 9 presents the equivalent circuit fitting of the impedance spectra, $R_s[C_1(R_1O_1)](R_2\text{CPE})$, which was used for all the DSSCs. R_s is the series

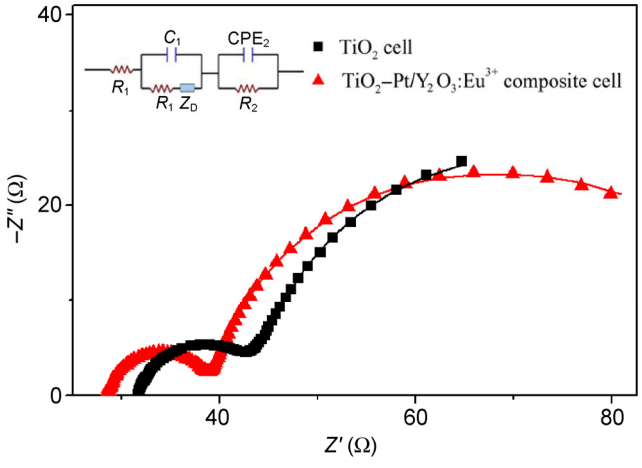

Figure 9 Nyquist plots of DSSCs comprised of pure TiO_2 cell and TiO_2–Pt/Y_2O_3:Eu^{3+} composite cell.

resistance, corresponding to the sheet resistance of the FTO glass, contact resistance, and wire resistance. R_2 represents the charge-transfer resistance between the photoelectrode–dye|I_3^-/I^- electrolyte interface. Z_{Dif} represents the finite-length Warburg impedance. The impedance of the finite-length Warburg diffusion is expressed as

$$Z_{Dif} = R_{Dif} \frac{\tanh(j\omega\tau)^{1/2}}{(j\omega\tau)^{1/2}} \quad (1)$$

where $R_{Dif} = B/Y_0$ and $\tau = B^2$. B is a constant phase element.

Based on the equivalent circuit, the EIS data obtained by fitting the impedance spectra of the composite DSSCs are listed in Table 2. R_2 is 30.32 Ω for the pure TiO_2 cell and 28.51 Ω for the TiO_2–Pt/Y_2O_3:Eu^{3+} composite cell. The lower interfacial resistance can result in higher interfacial electron transfer, which is a beneficial factor for enhanced photoelectric conversion efficiency. In addition, R_s for the pure TiO_2 cell and TiO_2–Pt/Y_2O_3:Eu^{3+} cell are separately 31.81 and 28.75 Ω, indicating that the incorporation of Pt/Y_2O_3:Eu^{3+} is beneficial for the interfacial electron transfer of FTO|TiO_2.

The electron recombination time (τ_n), electron transport time (τ_d), and charge collection efficiency (η_{cc}) are important factors determining the performance of DSSCs. IMPS and IMVS are conventional methods used to investigate the electron transfer and recombination process. The IMPS and IMVS response plots of the pure TiO_2 cell and TiO_2–Pt/Y_2O_3:Eu^{3+} composite cell are presented in Fig. 10. Compared with the pure TiO_2 cell, the TiO_2–Pt/Y_2O_3:Eu^{3+} composite cell has a longer τ_n and shorter τ_d. A shorter τ_d and longer τ_n are beneficial for enhancing photoelectric properties.

Table 2 Parameters obtained by fitting the impedance spectra of the composite solar cells using the equivalent circuit in the inset of Fig. 9

DSSCs	R_s (Ω)	C_1 (F)	R_1 (Ω)	Y_{o1} (S)	B ($s^{1/2}$)	R_2 (Ω)	CPE
Pure TiO_2	31.81	1.788×10^{-5}	8.57	0.00817	0.2269	30.32	0.001425
TiO_2–Pt/Y_2O_3:Eu^{3+}	28.75	4.714×10^{-6}	8.88	0.01439	0.4404	28.51	0.0008419

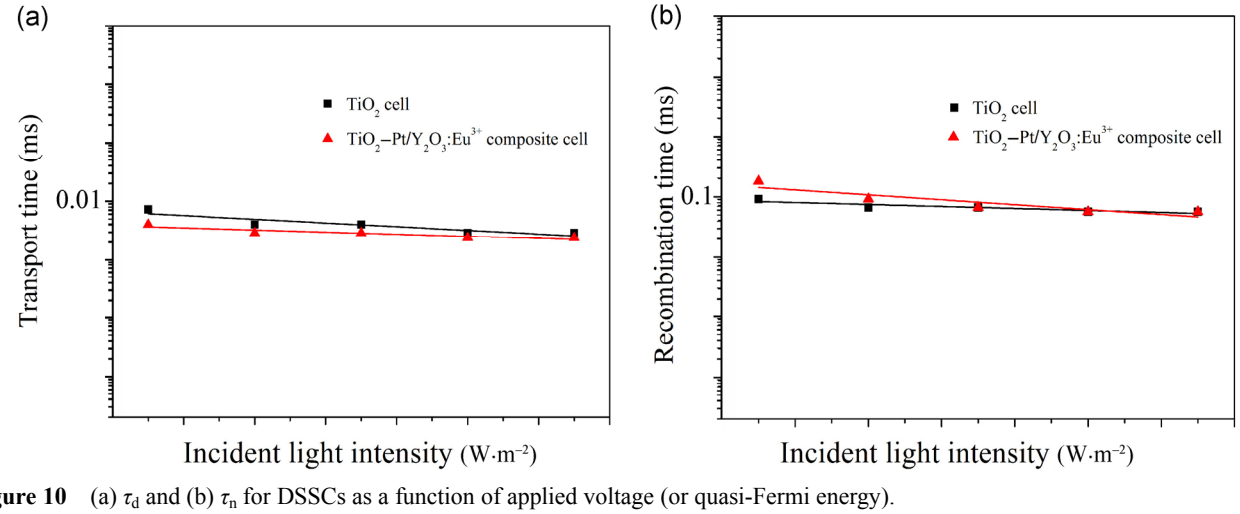

Figure 10 (a) τ_d and (b) τ_n for DSSCs as a function of applied voltage (or quasi-Fermi energy).

The η_{cc} values of the DSSCs were determined using the relation $\eta_{cc} = 1 - \tau_d/\tau_n$. Figure S5 in the ESM shows the η_{cc} values of the pure TiO_2 cell and TiO_2–$Pt/Y_2O_3:Eu^{3+}$ cell. The TiO_2–$Pt/Y_2O_3:Eu^{3+}$ composite cell has a higher η_{cc} than the pure TiO_2 cell. All these results indicate that the performance of the solar cells can be improved with the addition of $Pt/Y_2O_3:Eu^{3+}$.

4 Conclusions

In summary, we successfully synthesized $Y_2O_3:Eu^{3+}$ and $Pt/Y_2O_3:Eu^{3+}$ composite nanotubes using a combination of hydrothermal, vacuum extraction, and annealing processes. The luminescence intensity of $Y_2O_3:Eu^{3+}$ was enhanced by hybridization with Pt nanoparticles. The obtained $Pt/Y_2O_3:Eu^{3+}$ was used to design TiO_2–$Pt/Y_2O_3:Eu^{3+}$ composite photoanodes, and the photoelectric conversion efficiency was greatly enhanced with the incorporation of $Pt/Y_2O_3:Eu^{3+}$. The EIS results revealed that the interfacial resistance of the TiO_2–dye$|I_3^-/I^-$ electrolyte interface of the TiO_2–$Pt/Y_2O_3:Eu^{3+}$ composite cell was much smaller than that of the pure TiO_2 cell. In addition, the TiO_2–$Pt/Y_2O_3:Eu^{3+}$ composite cell exhibited a longer τ_n and shorter τ_d than the pure TiO_2 cell. The enhancement of the efficiency of the TiO_2–$Pt/Y_2O_3:Eu^{3+}$ composite cell was also related to the enhanced photoluminescence of the $Pt/Y_2O_3:Eu^{3+}$ composite nanotubes.

Acknowledgements

This work was supported by the National Natural Science Foundation of China (No. 21471050) and Heilongjiang Province Natural Science Foundation of Key Projects (No. ZD201301).

Electronic Supplementary Material: Supplementary material (the EDX spectrum and charge collection efficiency for DSSCs) is available in the online version of this article at http://dx.doi.org/10.1007/s12274-016-1120-z.

References

[1] Wang, X.; Zhuang, J.; Peng, Q.; Li, Y. D. A general strategy for nanocrystal synthesis. *Nature* **2005**, *437*, 121–124.

[2] Zhou, J.; Liu, Q.; Feng, W.; Sun, Y.; Li, F. Y. Upconversion luminescent materials: Advances and applications. *Chem. Rev.* **2015**, *115*, 395–465.

[3] Li, G. G.; Tian, Y.; Zhao, Y.; Lin, J. Recent progress in luminescence tuning of Ce^{3+} and Eu^{2+}-activated phosphors for pc-WLEDs. *Chem. Soc. Rev.* **2015**, *44*, 8688–8713.

[4] Zhang, J.; Yuan, Y.; Wang, Y.; Sun, F. F.; Liang, G. L.; Jiang, Z.; Yu, S. H. Microwave-assisted synthesis of photoluminescent glutathione-capped Au/Ag nanoclusters: A unique sensor-on-a-nanoparticle for metal ions, anions, and small molecules. *Nano Res.* **2015**, *8*, 2329–2339.

[5] Lin, L. W.; Sun, X. Y.; Jiang, Y.; He, Y. H. Sol-hydrothermal synthesis and optical properties of Eu^{3+}, Tb^{3+}-codoped one-dimensional strontium germanate full color nano-phosphors *Nanoscale* **2013**, *5*, 12518–12531.

[6] Kaczmarek, A. M.; van Hecke, K.; van Deun, R. Nano- and micro-sized rare-earth carbonates and their use as precursors and sacrificial templates for the synthesis of new innovative materials. *Chem. Soc. Rev.* **2015**, *44*, 2032–2059.

[7] Xia, Z. G.; Liu, R. S. Tunable blue-green color emission and energy transfer of $Ca_2Al_3O_6F:Ce^{3+}$, Tb^{3+} phosphors for near-UV white LEDs. *J. Phys. Chem. C* **2012**, *116*, 15604–15609.

[8] Binnemans, K. Lanthanide-based luminescent hybrid materials. *Chem. Rev.* **2009**, *109*, 4283–4374.

[9] Gai, S. L.; Li, C. X.; Yang, P. P.; Lin, J. Recent progress in rare earth micro/nanocrystals: Soft chemical synthesis, luminescent properties, and biomedical applications. *Chem. Rev.* **2014**, *114*, 2343–2389.

[10] Wang, F.; Tan, W. B.; Zhang, Y.; Fan, X. P.; Wang, M. Q. Luminescent nanomaterials for biological labelling. *Nanotechnology* **2006**, *17*, R1.

[11] Blasse, G.; Grabmaier, B. C. Energy transfer. In *Luminescent Materials*; Springer: Berlin, Heidelberg, 1994; pp 91–107.

[12] Nelson, J. A.; Brant, E. L.; Wagner, M. J. Nanocrystalline Y_2O_3: Eu phosphors prepared by alkalide reduction. *Chem. Mater.* **2003**, *15*, 688–693.

[13] Wang, L. M.; Li, X. Y.; Li, Z. Q.; Chu, W. S.; Li, R. F.; Lin, K.; Qian, H. S.; Wang, Y.; Wu, C. F.; Li, J. et al. A new cubic phase for a $NaYF_4$ host matrix offering high upconversion luminescence efficiency. *Adv. Mater.* **2015**, *27*, 5528–5533.

[14] Hebbink, G. A.; Stouwdam, J. W.; Reinhoudt, D. N.; van Veggel, F. C. J. M. Lanthanide(III)-doped nanoparticles that emit in the near-infrared. *Adv. Mater.* **2002**, *14*, 1147–1150.

[15] Buch, Z.; Kumar, V.; Mamgain, H.; Chawla, S. Silver nanoprism enhanced fluorescence in $YVO_4:Eu^{3+}$ nanoparticles. *Chem. Commun.* **2013**, *49*, 9485–9487.

[16] Lupan, O.; Viana, B.; Pauporté, T.; Dhaouadi, M.; Pellé, F.; Devys, L.; Gacoin, T. Controlled mixed violet–blue–

red electroluminescence from Eu: Nano-phosphors/ZnO-nanowires/p-gan light-emitting diodes. *J. Phys. Chem. C* **2013**, *117*, 26768−26775.

[17] Li, M.; Selvin, P. R. Luminescent polyaminocarboxylate chelates of terbium and europium: The effect of chelate structure. *J. Am. Chem. Soc.* **1995**, *117*, 8132–8138.

[18] Yang, D.; Yang, G. X.; Wang, X. M.; Lv, R. C.; Gai, S. L.; He, F.; Gulzar, A.; Yang, P. P. Y_2O_3:Yb, Er@mSiO_2–Cu_xS double-shelled hollow spheres for enhanced chemo-/photothermal anti-cancer therapy and dual-modal imaging. *Nanoscale* **2015**, *7*, 12180–12191.

[19] Zhang, F.; Braun, G. B.; Shi, Y. F.; Zhang, Y. C.; Sun, X. H.; Reich, N. O.; Zhao, D. Y.; Stucky, G. Fabrication of Ag@SiO_2@Y_2O_3:Er nanostructures for bioimaging: Tuning of the upconversion fluorescence with silver nanoparticles. *J. Am. Chem. Soc.* **2010**, *132*, 2850–2851.

[20] Su, J. M.; Wang, G. F.; Li, Y.; Li, R.; Xu, B. Y.; Wang, Y. P.; Zhang, J. S. Synthesis, novel luminescence properties, and surface-enhanced Raman scattering of Au/Y_2O_3:Eu^{3+} composite nanotubes. *Dalton Trans.* **2014**, *43*, 14720–14725.

[21] O'Regan, B.; Grätzel, M. A low-cost, high-efficiency solar cell based on dye-sensitizedcolloidal TiO_2 films. *Nature* **1991**, *353*, 737–740.

[22] Mathew, S.; Yella, A.; Gao, P.; Humphry-Baker, R.; Curchod, B. F. E.; Ashari-Astani, N.; Tavernelli, I.; Rothlisberger, U.; Nazeeruddin, M. K.; Grätzel, M. Dye-sensitized solar cells with 13% efficiency achieved through the molecular engineering of porphyrin sensitizers. *Nat. Chem.* **2014**, *6*, 242–247.

[23] Zhang, Y.; Zhang, B.; Peng, X.; Liu, L.; Dong, S.; Lin, L. P.; Chen, S.; Meng, S. X.; Feng, Y. Q. Preparation of dye-sensitized solar cells with high photocurrent and photovoltage by using mesoporous titanium dioxide particles as photoanode material. *Nano Res.* **2015**, *8*, 3830–3841.

[24] Brown, M. D.; Suteewong, T.; Kumar, R. S.; D'Innocenzo, V.; Petrozza, A.; Lee, M. M.; Wiesner, U.; Snaith, H. J. Plasmonic dye-sensitized solar cells using core–shell metal−insulator nanoparticles. *Nano Lett.* **2011**, *11*, 438–445.

[25] Wu, W. Q.; Xu, Y. F.; Rao, H. S.; Feng, H. L.; Su, C. Y.; Kuang, D. B. Constructing 3D branched nanowire coated macroporous metal oxide electrodes with homogeneous or heterogeneous compositions for efficient solar cells. *Angew. Chem., Int. Ed.* **2014**, *53*, 4816–4821.

[26] Nazeeruddin, M. K.; Kay, A.; Rodicio, I.; Humphry-Baker, R.; Mueller, E.; Liska, P.; Vlachopoulos, N.; Graetzel, M. Conversion of light to electricity by cis-X_2bis(2,2'-bipyridyl-4,4'-dicarboxylate)ruthenium(II) charge-transfer sensitizers (X = Cl–, Br–, I–, CN–, and SCN–) on nano-crystalline titanium dioxide electrodes. *J. Am. Chem. Soc.* **1993**, *115*, 6382–6390.

[27] Kim, S.; Lee, J. K.; Kang, S. O.; Ko, J.; Yum, J. H.; Fantacci, S.; De Angelis, F.; Di Censo, D.; Nazeeruddin, M. K.; Gratzel, M. Molecular engineering of organic sensitizers for solar cell applications. *J. Am. Chem. Soc.* **2006**, *128*, 16701–16707.

[28] Wang, M. K.; Chamberland, N.; Breau, L.; Moser, J. E.; Humphry-Baker, R.; Marsan, B.; Zakeeruddin, S. M.; Grätzel, M. An organic redox electrolyte to rival triiodide/iodide in dye-sensitized solar cells. *Nat. Chem.* **2010**, *2*, 385–389.

[29] Thapa, A.; Zai, J. T.; Elbonhy, H.; Poudel, P.; Adhikari, N.; Qian, X. F.; Qiao, Q. Q. TiO_2 coated urchin-like SnO_2 microspheres for efficient dye-sensitized solar cells. *Nano Res.* **2014**, *7*, 1154–1163.

[30] Yoo, D.; Kim, J.; Kim, J. H. Direct synthesis of highly conductive poly(3,4-ethylenedioxythiophene):poly(4-styrenesulfonate) (PEDOT:PSS)/graphene composites and their applications in energy harvesting systems. *Nano Res.* **2014**, *7*, 717–730.

[31] Liang, C. H.; Liu, C. S.; Li, F. B.; Wu, F. The effect of Praseodymium on the adsorption and photocatalytic degradation of azo dye in aqueous Pr^{3+}-TiO_2 suspension. *Chem. Eng. J.* **2009**, *147*, 219–225.

[32] Shi, J. W.; Zheng, J. T.; Wu, P. Preparation, characterization and photocatalytic activities of holmium-doped titanium dioxide nanoparticles. *J. Hazard. Mater.* **2009**, *161*, 416–422.

[33] Smith, W.; Mao, S.; Lu, G. H.; Catlett, A.; Chen, J. H.; Zhao, Y. P. The effect of Ag nanoparticle loading on the photocatalytic activity of TiO_2 nanorod arrays. *Chem. Phys. Lett.* **2010**, *485*, 171–175.

[34] Fang, X. L.; Li, M. Y.; Guo, K. M.; Zhu, Y. D.; Hu, Z. Q.; Liu, X. L.; Chen, B. L.; Zhao, X. Z. Improved properties of dye-sensitized solar cells by incorporation of graphene into the photoelectrodes. *Electrochim. Acta* **2012**, *65*, 174–178.

[35] Xu, F.; Chen, J.; Wu, X.; Zhang, Y.; Wang, Y. X.; Sun, J.; Bi, H. C.; Lei, W.; Ni, Y. R.; Sun, L. T. Graphene scaffolds enhanced photogenerated electron transport in ZnO photoanodes for high-efficiency dye-sensitized solar cells. *J. Phys. Chem. C* **2013**, *117*, 8619–8627.

[36] Wang, G. F.; Li, Y.; Jiang, B. J.; Pan, K.; Fan, N. Y.; Feng, Q. M.; Chen, Y. J.; Tian, C. G. *In situ* synthesis and photoluminescence of Eu^{3+} doped $Y(OH)_3$@β-$NaYF_4$ core–shell nanotubes. *Chem. Commun.* **2011**, *47*, 8019–8021.

[37] Wang, P.; Dai, Q.; Zakeeruddin, S. M.; Forsyth, M.; MacFarlane, D. R.; Grätzel, M. Ambient temperature plastic crystal electrolyte for efficient, all-solid-state dye-sensitized solar cell. *J. Am. Chem. Soc.* **2004**, *126*, 13590–13591.

[38] Hagfeldt, A.; Grätzel, M. Molecular photovoltaics. *Acc. Chem. Res.* **2000**, *33*, 269–277.